Applied Radiation and Isotopes 167 (2021) 109353

Contents lists available at ScienceDirect

Applied Radiation and Isotopes

journal homepage: http://www.elsevier.com/locate/apradiso

Colocalization of tracks from boron neutron capture reactions and images of isolated cells

Ian Postuma [a,*], Patrizia Sommi [b], Agostina Vitali [c], Diyun Shu [d], Greta di Martino [c], Laura Cansolino [a,e], Cinzia Ferrari [a,e], Vittorio Ricci [b], Chiara Magni [a,f], Nicoletta Protti [a], Setareh Fatemi [a], Umberto Anselmi Tamburini [c], Silva Bortolussi [a,f], Saverio Altieri [a,f]

[a] Istituto Nazionale di Fisica Nucleare sez, di Pavia, Via Agostino Bassi 6, Pavia, 27100, Italy
[b] Department of Molecular Medicine, Human Physiology Unit, University of Pavia, Corso Strada Nuova 65, Pavia, 27100, Italy
[c] Department of Chemistry, University of Pavia, Corso Strada Nuova 65, Pavia, 27100, Italy
[d] Department of Nuclear Science and Technology, Nanjing University of Aeronautics and Astronautics, Yudao Street 29, Nanjing, 210016, China
[e] Department of Clinic-Surgical Sciences, Experimental Surgery Laboratory, University of Pavia, via Ferrata 9, 27100, Pavia, Italy
[f] Department of Physics, University of Pavia, Corso Strada Nuova 65, Pavia, 27100, Italy

ARTICLE INFO

Keywords:
BNCT
Neutron autoradiography
Boron
Cell cultures

ABSTRACT

In Boron Neutron Capture Therapy, the boronated drug plays a leading role in delivering a lethal dose to the tumour. The effectiveness depends on the boron macroscopic concentration and on its distribution at sub-cellular level. This work shows a way to colocalize alpha particles and lithium ions tracks with cells. A neutron autoradiography technique is used, which combines images of cells with images of tracks produced in a solid-state nuclear track detector.

1. Introduction

Neutron Capture Therapy (NCT) is an oncological treatment, that uses thermal neutrons along with atoms having high neutron capture cross section. The most used isotope in NCT is boron-10, i.e. Boron Neutron Capture Therapy (BNCT). The reaction between low energy neutrons and ^{10}B produces an alpha particle and a lithium ion. The energy released by this reaction is approximately 2.8 MeV and it is deposited in a range similar to the cell diameter (Barth, 2003). Therefore, the dose will be localized in and around those cells which uptake boron. For this reason, the selectivity of BNCT is due to the biological targeting of the chemical compounds carrying the boron atoms. To date, only three boron compounds have been clinically used: sodium borocaptate (BSH), boronophenylalanine (BPA) and Sodium Decaborate (GB-10) (Barth et al., 2018; Trivillin et al., 2019). The BNCT community is actively investigating for new compounds able to increase the efficacy of the therapy, by searching for new formulations which increase the boron concentration ratio between malignant and healthy tissue. Moreover, BNCT effect on tumour improves if boron atoms are located inside the cell nucleus, so that the probability of damaging the DNA by charged particle crossing is higher. Thus, different sub-cellular ^{10}B distributions in the same cell type/morphology and at the same macroscopic ^{10}B concentration cause different BNCT effectiveness. The Compound Biological Effectiveness (CBE) was introduced to measures this characteristic, and it is defined as: the ratio of the dose of a gamma reference radiation and the BNCT dose to obtain the same biological outcome (Ono, 2016; Sato et al., 2018). Usually, the observed outcome is cell survival, consequently higher CBE corresponds to a higher cell killing efficacy. In synthesis, the value of CBE depends on the ability of the compound to reach sensitive targets in the tumour cells. One possible method to infer the compound effectiveness is to identify how boron atoms distribute at sub-cellular level. There are many experimental methods capable of measuring the average boron concentration in tissues or liquid samples (Pollmann et al., 1993; Riley and Harling, 1996; Alfassi and Probst, 1999; Bortolussi et al., 2010; Probst, 1999; Portu et al., 2015). This average ^{10}B concentration does not describe the way boron distributes at sub-cellular level. Therefore, other methodologies were developed to characterize boron distribution within the cell membrane (Chandra et al., 2014; Wittig et al., 2008; Fartmann et al., 2004; Chandra, 2003; Portu et al., 2016; Tanaka et al., 2014). In this work, we show a technique consisting in overlapping an optical image of cells and the optical image of tracks (of alpha particles and lithium ions

* Corresponding author.
E-mail address: ian.postuma@pv.infn.it (I. Postuma).

https://doi.org/10.1016/j.apradiso.2020.109353
Received 30 August 2019; Received in revised form 7 July 2020; Accepted 21 July 2020
Available online 4 October 2020

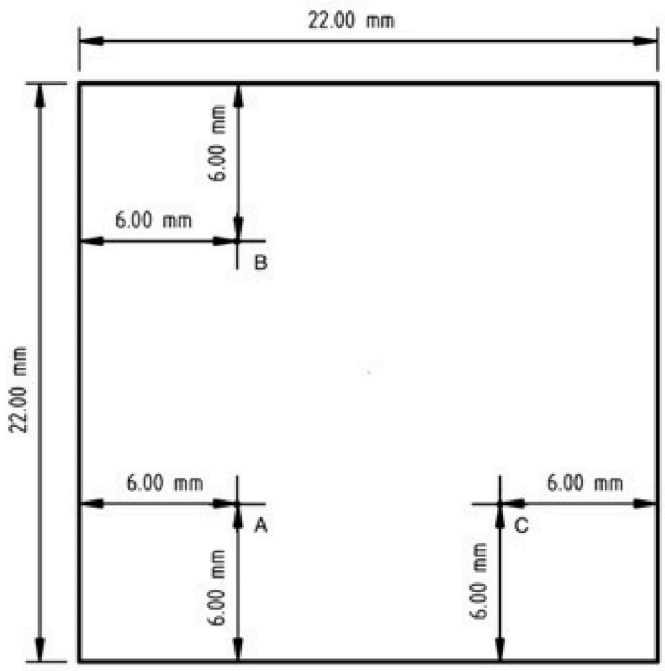

Fig. 1. CR-39 dimensions and 60 μm reference marks positions inside the CR-39.

coming from the boron neutron capture reaction), obtained by a semi-standard neutron autoradiography technique.

2. Material and methods

The autoradiography technique described in this work is based on a CR-39 detector, which is a passive Solid-State Nuclear Track Detector (SSNTD). Cells are grown directly on a CR-39 to 50% confluency, i.e. avoiding vertical overlapping cells. Then cells are treated with boron and, at the end of the contact time, the detector is washed from the culture medium, and the cells are fixed. At this point, optical images of cells are taken, using a microscope with a motorized stage which has the capability to record the coordinates of a region of interest (ROI), i.e. the image. Afterwards, the detector is irradiated in the thermal column of the nuclear research reactor TRIGA Mark II of the University of Pavia (LENA laboratory). During the irradiation, alpha particles and lithium ions from the neutron capture reaction on ^{10}B may reach and damage the surface of the CR-39. To optically visualize these latent tracks, the SSNTD is chemically etched and, by using again the motorized stage, the detector is repositioned to the same ROIs where the optical image of the cell was taken (although no cells are now visible). The recorded track image is finally overlaid over the cells image to visualize track distribution inside the cell structures.

2.0.1. CR-39 preparation

The SSNTD is cut into squares of 22 mm per side. Three reference marks with a diameter of 60 μm are drilled into the detector 6.00 mm from the CR-39 border, as shown in Fig. 1. CR-39 is sterilized in ethanol for 4 h and then preconditioned in cell culture medium for the cell growth.

2.0.2. Cells treatment

HeLa cells, epithelial cells derived from human cervical cancer cells, are maintained in Dulbecco's modified Eagle's medium with 10% fetal bovine serum and 2 mM L-glutamine (Lonza, Basel, Switzerland) at 37°C in a humidified atmosphere of 5% CO_2 in air. Cells are seeded directly on CR-39. At about 50% confluence, cells are exposed to BPA at a concentration of 80 ppm of ^{10}B for 4 h. This treatment time and concentration gives a good boron uptake while keeping a low cytotoxicity (Ferrari et al., 2011). At the end of treatment, cells are washed at least three times with phosphate buffer saline (PBS) and fixed with 4% paraformaldehyde for 15 min at room temperature. The PBS washing solution is routinely used for *in-vitro* boron uptake experiments, to remove the unbound BPA without altering intracellular concentration levels (Ferrari et al., 2011). Finally, the substrate with the cells is mounted with a coverslip.

2.0.3. Optical images of cells

The CR-39 with treated cells is positioned under an inverted microscope (Olympus IX83 equipped with 10X, 20X and 60X objectives and motorized Märzhäuser stage). The microscope is connected and operated from a PC through the Olympus CellSens Software. This enables the readout of the stage position through the X–Y coordinate,s which refers to the top left corner of the microscopic image. These coordinates define the ROI.

At the start, the coordinates of 3 points marked on the CR-39 are stored in an ASCII file, as a reference for later re-positioning. Subsequently, cell images are acquired, and the coordinates of the relative ROI recorded in the same ASCII file.

2.1. Irradiation

The irradiation set-up is the same as the one described in (Gadan et al., 1016; Postuma et al., 1016), where the samples are positioned inside a plexiglass case and then introduced into the Thermal Column reactor, in a position where the thermal neutron flux at maximum power (250 kW) is about $1.37{\cdot}10^{9}$ cm^{-2} s^{-1}. Once inserted, the samples are irradiated with a neutron fluence of $9.8 \pm 0.5 \cdot 10^{12}$ cm^{-2} (Gadan et al., 1016).

2.2. Etching

After the irradiation, the coverslip is removed and the SSNTD is etched in a 6.25 N NaOH solution at 70 °C for 20 min (i.e. a bulk etching of approximately 500 nm), that enlarges the latent tracks produced in the detector by high LET charged particles from neutron capture in boron. The track distribution is then acquired using the image acquisition system described in Section 2.0.3. The obtained track pictures are subsequently matched with the images containing cells, using an algorithm written specifically for this purpose (see below).

2.3. Alpha and lithium tracks from neutron capture reaction on boron

During neutron irradiation, the CR-39 is exposed to a mixed field of charge particles. The most abundant high LET particles are alpha and lithium ions from the neutron capture reaction on boron. Other particles that may produce tracks are protons from the neutron capture reaction on nitrogen and from neutron scattering on hydrogen. Previous work has shown that, with this neutron fluence and these etching conditions, proton tracks are smaller than alpha and lithium tracks (Altieri et al., 2008; Gadan et al., 1016). In fact, alpha and lithium particles have LET values which are at least 4 times higher than LET of protons (Ziegler et al., 2010), thus causing greater damage to the detector structure resulting in a larger track after the etching (Spurny' et al., 1996). This difference allows the selection of tracks generated by boron reactions based on their diameter. A Scanning Electron Microscope (SEM) was used to better evaluate the size of the tracks originated by alpha and lithium ions from the neutron capture reaction on boron. For this purpose a TESCAN Mira 3 XMU SEM was used, where the surface of the CR-39 was coated with a thin layer of graphite (few nm) by vacuum

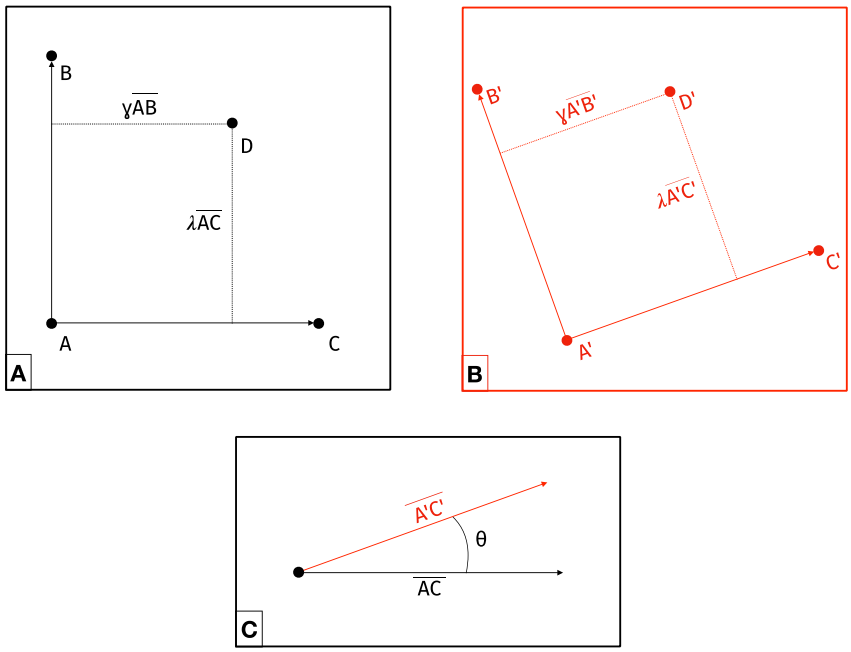

Fig. 2. A schematic example of the reference system reconfiguration. The Reference mark points are defined as A, B and C. The cell ROI point is D. Scheme A) is the initial configuration (used for cell images). Scheme B) is the hypothetical reference system position after the etching, when re-positioned under the microscope (used for track images). Scheme C) shows θ, which is the angle between $\overline{AC}$ and $\overline{A'C'}$.

evaporation. The CR-39 sample used for this analysis was irradiated with thermal neutrons coupled to a boron standard implanted in a silicon support (NIST-Standard Reference Material 2137) and then etched following the condition described in the previous section.

2.3.1. Repositioning algorithm

A Python script was written to match the cell position with the track position. The algorithm requires as input the coordinates of 3 reference points, as shown in Fig. 2A: $\overline{A},\overline{B},\overline{C}$. These points refer to the microscope stage coordinate system and are defined by positioning the reference marks at the center of the Field of View (FoV). The centering can be performed since the marks have a circular shape, thus it is possible to calculate and record their centre coordinates. The error related to the determination of the centre coordinates is negligible compared to the precision of the microscope motorized stage that is 1 μm. Once a single spot is centered in the FoV, its coordinates refers to the top left corner of the picture. For convention, all the coordinates given by the microscope stage, refer to the top left corner of the acquired ROI.

The next input of the script is the cells image coordinate $\overline{D}$, which is related to the reference points by equation (1). This point is stored when the optical image of the cell is acquired.

$$\overline{AD} = \lambda\overline{AB} + \gamma\overline{AC} \tag{1}$$

It is now possible to solve equation (1) and to compute λ and γ; this calculation is performed by using the fsolve function defined in Scipy (Oliphant, 2007), a Python module used for scientific computation. When the CR-39 is repositioned, as represented in Fig. 2B, on the stage after the etching, the coordinates of the reference points are re-evaluated $\overline{A'},\overline{B'},\overline{C'}$. The advantage of using circular marks is that the center of the circle is not affected by the etching of the SSNTD. Therefore, the re-evaluated reference points together with the computed λ and γ values, are used inside the script to relocate the cell image position through Equation (2). Equation (3) was used to calculate the rotation angle θ when repositioning the CR-39 (i.e. the dot product), while the cross product $\overline{A'C'} \times \overline{AC}$ was used to determine the sense of rotation, as shown in Fig. 2C. Since we can consider $\overline{AC}$ and $\overline{A'C'}$ to lie in the XY plane, the resulting cross product vector is parallel to the z-axis. Consequently, a positive z value coincides to an anticlockwise rotation while a negative value defines a clockwise rotation.

$$\overline{D'} = \lambda\overline{B'} + \gamma\overline{C'} + (1-\lambda-\gamma)\overline{A'} \tag{2}$$

$$\cos\theta = \frac{\overline{AC}\cdot\overline{A'C'}}{\left|\overline{AC}\right|^2};\ \left|\overline{AC}\right| = \left|\overline{A'C'}\right| \tag{3}$$

At this point, the microscope stage can be repostioned in the FoV containing the same ROI of the cells optical image, now defined by $\overline{D'}$, which is the first output of the Python script. The second output is the rotation angle which can be used to precisely overlay the optical images. The accuracy of the overlay depends on the precision of the microscope stage movement.

As a validation of the algorithm and to assess the accuracy of the reposition method, a CR-39 with a mark was positioned under the microscope. The reference points were acquired and the mark ROI was recorded. Then the CR-39 was removed and re-positioned. The ROI position was then calculated using the method described in this paragraph.

2.3.2. Track imaging and overlay

Once the CR-39 is etched and repositioned on the microscope stage, the reference marks coordinates are gathered. Then, by means of the repositioning algorithm, the cells' ROI coordinates are computed.

These resulting new coordinates are then inserted into the stage/microscope controlling software, and the images of these regions are taken. Once the optical images of cells and tracks are gathered, the corresponding ROIs are overlaid with Fiji (Schindelin et al., 2012), a scientific image processing package of ImageJ.

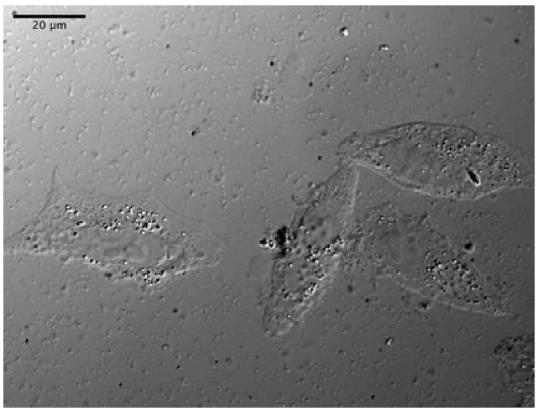

Fig. 3. Optical image (60x) of HeLa cells on CR-39.

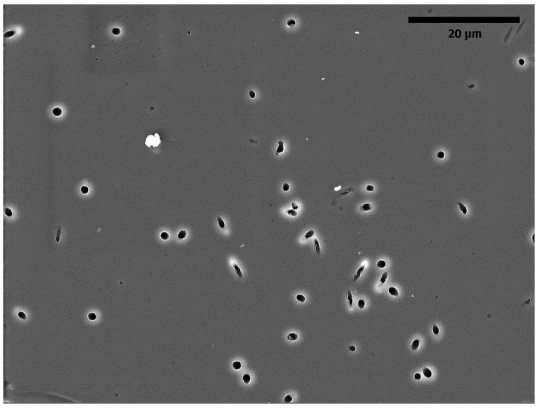

Fig. 4. SEM image of the etched CR-39 which was irradiated coupled to a NIST standard containing ^{10}B. The Black spots are tracks from helium and lithium ions with a diameter of approximately 1 μm.

3. Results and discussion

Fig. 3 shows an optical image of HeLa cells grown on a CR-39. As a result, cell growth on CR-39 can be considered similar to the growth on polystyrene Petri dishes commonly used for cell culture. No changes in cell morphology or growth rate were noticed as cells attached and spread normally on the CR-39 surface. Moreover, cells did not show any sign of suffering (blebbing, rounding, etc.) and detachment, which are typical in the case of poor compatibility with surface material. Overall the cell appearance was normal. The image was taken with DIC (Differential Interference Contrast) which gives the cells a pseudo-3D aspect; because of the different refractive index, internal structures appear as bumps or irregularities. This is the reason why the cells have those "black dots", that are most likely cytoplasmic vesicles.

Fig. 4 shows the SEM image of the CR-39 irradiated with the NIST standard. The black dots are alpha particle and lithium ion tracks. The mean diameter of the rounder pits is approximately 1 μm.

Fig. 5A shows a flaw on the CR-39 surface, the ROI of this flaw was used to test the re-positioning method. Fig. 5B shows the result of the repositioning of the CR-39. The red contour shows the flaw borders of the initial ROI reference points, while the overlayed blue line is the same flaw taken with the ROI computed through the re-positioning algorithm. It is evident that the method is accurate enough to be used for tracks and cell colocalization.

Fig. 1 shows the CR-39 layout with the drilled holes position. As described in the previous paragraph, this SSNTD was directly used as a substrate for the cell growth. Once the cells had reached the desired confluence level they were fixed, and images were taken. Before taking

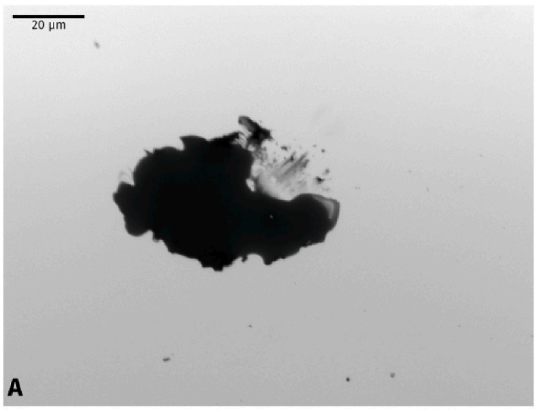

Fig. 5. Optical images (60x) of a flaw on the CR-39 surface, used as ROI to show the accuracy of the re-positioning method. Scheme A is the flaw image. Scheme B is the overlap of the edges of two images taken after re-positioning the CR-39.

Fig. 6. Optical image (60x) of tracks left on the CR-39 by alpha and lithium ions coming from the neutron capture reaction on ^{10}B.

the cell images the reference mark points $\overline{A}, \overline{B}, \overline{C}$ were recorded as shown in Fig. 2.

For the cell shown in Fig. 3, the coordinate point $\overline{D}$ was recorded. The set-up was irradiated and subsequently etched.

The CR-39 was then re-positioned on the optical microscope and the new positions of the same reference marks were recorded as $\overline{A'}, \overline{B'}, \overline{C'}$. These points were then fed into the Python script which returns the new ROI coordinate $\overline{D'}$, the rotation angle θ and the rotation direction. Fig. 6 shows the tracks of alpha particles and lithium ions produced by the neutron capture reaction in ^{10}B at point $\overline{D'}$. Track density is good enough to avoid too many overlapping tracks.

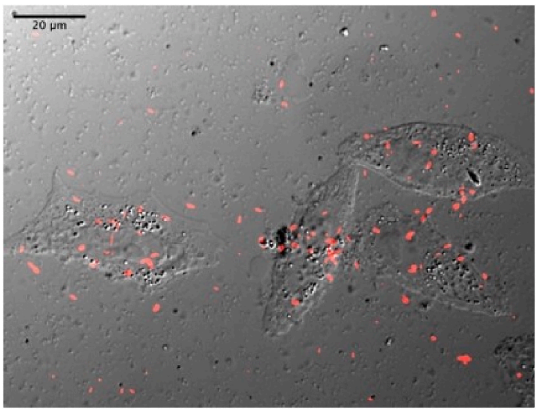

Fig. 7. Merge of the cell image with the tracks left in the CR-39.

Now Figs. 3 and 6 can be merged, and the result is shown in Fig. 7. The final overlaid image shows the superimposition of tracks and cells. Most of the tracks are within or around the cells, revealing that BPA was internalized. Anyhow, to determine the initial position of the boron compound, further work should be performed. One possibility is to measure the circularity of the tracks like in the work of Tanaka et al. (2014). In this way, it is possible to select perpendicularly penetrating tracks. These pits, once overlaid over the cell image, can be used to define the (x,y) coordinates of the boron atom on which the neutron capture reaction occurred, leaving the depth (i.e. the z coordinate) within the cell as an unknown quantity.

4. Conclusion

Even if further developments should be performed, the technique described in this work can be used to picture if ^{10}B is internalized into the cell and if it may reach recognizable cell structures. Consequently, giving a qualitative information on the boron carrier's ability to approach sensitive parts of the cell. Moreover, when a thermal neutron source is available, this technique is simple and affordable since microscopes with motorized stages are commonly available in a biology laboratory. An important feature of the method is that other types of images can be coupled to gather more information about the drug distribution. For example, if the carrier is labeled with a fluorescent probe, a third image can be recorded and overlaid with the same algorithm, to investigate also the properties of the carrier itself, not only of boron localization. Moreover, once the cells and the CR-39 are irradiated the cells can be coloured to highlight the internal structures, adding further details to the image stack. Future work is planned to further optimize the technique and to apply it to different cell cultures and different boron formulations, to point out differences in boron distribution and draw conclusions on the effectiveness of newly proposed drugs for BNCT.

Declaration of competing interest

The authors declare that they have no known competing financial interests or personal relationships that could have appeared to influence the work reported in this paper.

References

Alfassi, Z.B., Probst, T.U., 1999. On the calibration curve for determination of boron in tissue by quantitative neutron capture radiography. Nucl. Instrum. Methods Phys. Res., Sect. A: Accelerators, Spec250 trometers, Detectors and Associated Equipment 428 (2–3), 502–507.

Altieri, S., Bortolussi, S., Bruschi, P., Chiari, P., Fossati, F., Stella, S., Prati, U., Roveda, L., Zonta, A., Zonta, C., et al., 2008. Neutron autoradiography imaging of selective boron uptake in human metastatic tumours. Appl. Radiat. Isot. 66 (12), 1850–1855.

Barth, R.F., 2003. A critical assessment of boron neutron capture therapy: an overview. J. Neuro. Oncol. 62 (1–2), 1–5.

Barth, R.F., Mi, P., Yang, W., 2018. Boron delivery agents for neutron capture therapy of cancer. Canc. Commun. 38 (1), 35.

Bortolussi, S., Altieri, S., Protti, N., Stella, S., Ballarini, F., Bruschi, P., Gadan, M.A., Thorp, S.I., Miller, M., Pozzi, E.C.C., 2010. 10B measurement by alpha spectrometry and 10B imaging by neutron autoradiography as a contribution to the understanding of BNCT radiobiology in oral cancer and liver metastases animal models. In: Proceedings of the 14th. International Congress on Neutron Capture Therapy, pp. 59–62.

Chandra, S., 2003. SIMS ion microscopy as a novel, practical tool for subcellular chemical imaging in cancer research. Appl. Surf. Sci. 203, 679–683.

Chandra, S., Ahmad, T., Barth, R.F., Kabalka, G.W., 2014. Quantitative evaluation of boron neutron capture therapy (BNCT) drugs for boron delivery and retention at subcellular-scale resolution in human glioblastoma cells with imaging secondary ion mass spectrometry (SIMS). J. Microsc. 254 (3), 146–156.

Fartmann, M., Kriegeskotte, C., Dambach, S., Wittig, A., Sauerwein, W., Arlinghaus, H.F., 2004. Quantitative imaging of atomic and molecular species in cancer cell cultures with TOF-SIMS and Laser-SNMS. Appl. Surf. Sci. 231, 428–431.

Ferrari, C., Bakeine, J., Ballarini, F., Boninella, A., Bortolussi, S., Bruschi, P., Cansolino, L., Clerici, A., Coppola, A., Di Liberto, R., et al., 2011. In vitro and in vivo studies of boron neutron capture therapy: boron uptake/washout and cell death. Radiat. Res. 175 (4), 452–462.

M. Gadan, S. Bortolussi, I. Postuma, F. Ballarini, P. Bruschi, N. Protti, D. Santoro, S. Stella, L. Cansolino, A. Clerici, C. Ferrari, A. Zonta, C. Zonta, S. Altieri, Set-up and calibration of a method to measure ^{10}B concentration in biological samples by neutron autoradiography, Nucl. Instrum. Methods Phys. Res. Sect. B Beam Interact. Mater. Atoms 274. doi:10.1016/j.nimb.2011.11.043.

Oliphant, T.E., 2007. Python for scientific computing. Comput. Sci. Eng. 9 (3), 10–20.

Ono, K., 2016. An analysis of the structure of the compound biological effectiveness factor. J. Radiat. Res. 57 (S1) i83–i89.

Pollmann, D., Broekaert, J.A.C., Leis, F., Tschöpel, P., Tölg, G., 1993. Determination of boron in biological tissues by inductively coupled plasma optical emission spectrometry (ICP-OES). Fresen. J. Anal. Chem. 346 (4), 441–445.

Portu, A., Postuma, I., Gadan, M.A., Saint Martin, G., Olivera, M.S., Altieri, S., Protti, N., Bortolussi, S., 2015. Inter-comparison of boron concentration measurements at INFN-University of Pavia (Italy) and CNEA (Argentina). Appl. Radiat. Isot. 105, 35–39.

Portu, A.M., Rossini, A.E., Gadan, M.A., Bernaola, O.A., Thorp, S.I., Curotto, P., Pozzi, E. C.C., Cabrini, R.L., Saint Martin, G., 2016. Experimental set up for the irradiation of biological samples and nuclear track detectors with UV C. Rep. Practical Oncol. Radiother. 21 (2), 129–134.

I. Postuma, S. Bortolussi, N. Protti, F. Ballarini, P. Bruschi, L. Ciani, S. Ristori, L. Panza, C. Ferrari, L. Cansolino, S. Altieri, An improved neutron autoradiography set-up for ^{10}B concentration measurements in biological samples, Rep. Practical Oncol. Radiother. 21 (2). doi:10.1016/j.rpor.2015.10.006.

Probst, T.U., 1999. Methods for boron analysis in boron neutron capture therapy (BNCT). A review. Fresen. J. Anal. Chem. 364 (5), 391–403.

Riley, K.J., Harling, O.K., 1996. Boron-10 analyses using prompt gamma neutron activation and ICP-AES. Trans. Am. Nucl. Soc. 75, 31–32.

Sato, T., Masunaga, S.-i., Kumada, H., Hamada, N., 2018. Microdosimetric modeling of biological effectiveness for boron neutron capture therapy considering intra-and intercellular heterogeneity in 10 b distribution. Sci. Rep. 8 (1), 1–14.

Schindelin, J., Arganda-Carreras, I., Frise, E., Kaynig, V., Longair, M., Pietzsch, T., Preibisch, S., Rueden, C., Saalfeld, S., Schmid, B., 2012. Fiji: an opensource platform for biological-image analysis. Nat. Methods 9 (7), 676.

Spurný, F., Bednář, J., Johansson, L., Sätherberg, A., 1996. Linear energy transfer spectra of secondary particles in cr-39 track etch detectors. Radiat. Meas. 26 (5), 645–649.

Tanaka, H., Sakurai, Y., Suzuki, M., Masunaga, S.-i., Takamiya, K., Maruhashi, A., Ono, K., 2014. Development of a simple and rapid method of precisely identifying the position of 10b atoms in tissue: an improvement in standard alpha autoradiography. J. Radiat. Res. 55 (2), 373–380.

Trivillin, V.A., Serrano, A., Garabalino, M.A., Colombo, L.L., Pozzi, E.C., Hughes, A.M., Curotto, P.M., Thorp, S.I., Farías, R.O., González, S.J., et al., 2019. Translational boron neutron capture therapy (BNCT) studies for the treatment of tumors in lung. Int. J. Radiat. Biol. 95 (5), 646–654.

Wittig, A., Michel, J., Moss, R.L., Stecher-Rasmussen, F., Arlinghaus, H.F., Bendel, P., Mauri, P.L., Altieri, S., Hilger, R., Salvadori, P.A., 2008. Boron analysis and boron imaging in biological materials for boron neutron capture therapy (BNCT). Crit. Rev. Oncol.-Hematol. 68 (1), 66–90.

Ziegler, J.F., Ziegler, M.D., Biersack, J.P., 2010. Srim–the stopping and range of ions in matter. Nucl. Instrum. Methods Phys. Res. Sect. B Beam Interact. Mater. Atoms 268 (11–12), 1818–1823, 2010.